Materials Today Bio 30 (2025) 101399

Contents lists available at ScienceDirect

Materials Today Bio

journal homepage: www.journals.elsevier.com/materials-today-bio

A human skin-on-a-chip platform for microneedling-driven skin cancer treatment

Natan R. Barros [a,b,1,**], Raehui Kang [c,1], Jinjoo Kim [a], Menekse Ermis [a], Han-Jun Kim [a,e], Mehmet R. Dokmeci [a], Junmin Lee [a,c,d,f,*]

[a] Terasaki Institute for Biomedical Innovation (TIBI), Los Angeles, CA, 90024, USA
[b] National Laboratory of Bioscience (LNBio), National Center of Research in Energy and Materials (CNPEM), Campinas, 13083-100, Brazil
[c] Division of Interdisciplinary Bioscience & Bioengineering, Pohang University of Science and Technology (POSTECH), Pohang, 790-784, Republic of Korea
[d] Department of Materials Science and Engineering, Pohang University of Science and Technology (POSTECH), Pohang, 790-784, Republic of Korea
[e] College of Pharmacy, Korea University, Sejong, 30019, Republic of Korea
[f] Institute for Convergence Research and Education in Advanced Technology, Yonsei University, Incheon, 21983, Republic of Korea

ARTICLE INFO

Keywords:
Skin-on-a-chip
Bioprinting
Biofabrication
Microneedling
Skin cancer
Gelatin methacryloyl (GelMA)

ABSTRACT

Skin-on-a-chip models provide physiologically relevant platforms for studying diseases and drug evaluation, replicating the native skin structures and functions more accurately than traditional 2D or simple 3D cultures. However, challenges remain in creating models suitable for microneedling applications and monitoring, as well as developing skin cancer models for analysis and targeted therapy. Here, we developed a human skin/skin cancer-on-a-chip platform within a microfluidic device using bioprinting/bioengineering techniques. The fabricated skin models include vascular, dermal, and epidermal layers, demonstrating increased functionalities and maturation of dermal (Collagen I & Fibronectin for 7 days) as well as epidermal (Filaggrin & Keratin 10, 14, and 19 at the air-liquid interface (ALI) for 21 days) layers. Histological analysis confirmed the formation of a differentiated epidermis and ridges at the dermal-epidermal junction in our model, closely resembling native skin tissue. Melanoma cells were embedded approximately 400 μm beneath the epidermis to simulate tumor invasion into the dermis. The platform was further used to test doxorubicin (DOX)-loaded gelatin methacryloyl (GelMA) microneedles (MNs) for localized transdermal drug delivery targeting melanoma. The DOX-loaded MNs penetrated uniformly to a depth of approximately 600 μm, effectively reaching the melanoma cells. Drug delivery via MNs demonstrated significantly higher efficiency than diffusion through media flow, confirming the practicality and robustness of the proposed model for future therapeutic applications.

1. Introduction

Skin is the first defense barrier against environmental insults as well as a facile route for administering drugs [1–5]. The questionable biological relevance of animal models to humans, their high cost, and the ethical/regulatory requirements drive researchers to reduce/stop using animal tests, which has accelerated the race to develop human cell-based *in vitro* models [6–14]. To effectively mimic and predict *in vivo* events, essential skin functions must be replicated using appropriate *in vitro* models [15,16]. Previously, 2D cell cultures were used; however, these 2D models do not fully mimic *in vivo* skin physiology nor provide histological information, which is considered a gold standard for understanding skin function [15]. Alternatively, three-dimensional (3D) models such as reconstructed epidermis models integrating human cell lines or patient-derived cells have been proposed to replace animal testing [17–23]. However, these models have several limitations, including the absence of a dermal layer containing fibroblasts that affect the process of keratinocyte proliferation and terminal differentiation [16,24–26]; the absence of a vascular layer to increase the efficiency of nutrients and biomarkers transport and cell migration [27]; and the lack

* Corresponding author. Department of Materials Science and Engineering, Pohang University of Science and Technology (POSTECH), Pohang, 790-784, Republic of Korea.
** Corresponding author. Terasaki Institute for Biomedical Innovation (TIBI), Los Angeles, CA, 90024, USA.
E-mail addresses: natan.barros@lnbio.cnpem.br (N.R. Barros), junmin@postech.ac.kr (J. Lee).
[1] These authors equally contributed to this work.

https://doi.org/10.1016/j.mtbio.2024.101399
Received 19 September 2024; Received in revised form 6 December 2024; Accepted 9 December 2024
Available online 10 December 2024

of a dynamic interstitial fluid flow present in the tissue [28–30].

Recent advances in microfluidic systems have allowed the modeling of tissues and organs known as organs-on-a-chip [9,27,28,30,31]. Among these technologies, the development of skin-on-a-chip systems has the potential to offer relevant physiological models for studying diseases and drug evaluation [32–37]. For example, Abaci et al. developed a platform that could be used to maintain human skin equivalents for three weeks with proliferating keratinocytes (KCs) [32]. The small scale of the design allowed a 36-fold reduction in the quantity of required culture medium and cells compared to conventional Transwell cultures but also showed structures similar to those of *in vivo* skin. In another study, Ramaan et al. described a miniaturized *in vitro* 3D skin model with immune competence using immortalized human KCs and leukemic monocyte lymphoma cells [36]. This study demonstrated that the perfusion of culture media to cells notably enhanced the formation of tight junctions compared to static cultures. However, it is important to build a physiologically relevant skin model with a 3D cellular organization and natural tissue architectures since key *in vitro* functions and characteristics could vary with different tissue frameworks [21,38]. Thus, recapitulating native skin architectures *in vitro* would provide improved accuracy in therapeutic development [39,40]. For instance, a recent study by Sriram et al. developed a human skin equivalent by employing a fibrin-based dermal matrix combined with a fluidic system [41]. It was shown that perfusion and precise control of the microenvironment enabled enhanced epidermal morphogenesis, differentiation, and barrier function. Additionally, in a study by Lorthois et al., inflammatory cytokines like Tumor Necrosis Factor-alpha (TNF-α) and Interferon-gamma (IFN-γ) were applied to a three-dimensional skin model to develop a psoriasis skin model. This treatment resulted in epidermal thickening, abnormal epidermal differentiation, and inflammatory cell infiltration, effectively recapitulating an inflammatory environment by inducing T-cell chemotaxis [42].

The aforementioned skin-on-a-chip models are reported to be used for testing penetration and toxicity of chemicals, studying treatments, and modeling skin-related diseases [32,36,41–45]. However, studies on cosmetic and therapeutic agents, such as turmeric (Curcuma longa) and α-lipoic acid (ALA), often assess efficacy by delivering these compounds through microfluidic channels, rather than via direct epidermal absorption [46,47]. Moreover, testing a device applicable to the skin such as microneedles (MN), is still challenging because even 3D models of assembling multi-layer cells do not have enough mechanical strength as well as a thickness suitable for microneedling application and monitoring to withstand pressures to test MN patches [48]. Thus, a simple, time-efficient, robust, reliable, and scalable skin-on-a-chip platform is required for applications in physical therapies including physically exfoliating treatments that target localized skin problems.

In our previous work, we have employed biomaterial-based approaches and bioengineered techniques to develop a 3D skin model physiologically resembling *in vivo* skin structure [49]. Such was accomplished by constructing networks of bioprinted endothelium, a 3D dermis layer, and multilayered epidermis. Analysis of mechanical properties of gelatin methacryloyl (GelMA)-based bioinks mixed with different ratios of alginate revealed bioprinted endothelium could be better modeled to optimize endothelial cell viability with a mixture of 7.5 % GelMA and 2 % alginate. It was observed that matrix stiffness plays a crucial role in modulating produced levels of pro-collagen I alpha-1 and matrix metalloproteinase-1 in human dermal fibroblasts and affecting their viability, proliferation, and spreading. Moreover, seeding human KCs with gelatin-coating multiple times proved to help reduce culture time to create multiple layers of KCs while maintaining their viability.

Combining our previous methods of 3D skin models and microfluidics has shown that the design strategy allows building a skin model with a thickness suitable for microneedling application and monitoring in the presence of perfused media microchannels to supply nutrients and eliminate metabolic waste products, fibroblast-endothelial cells interactions to mimic the *in vivo* dermis niche, and air-liquid interface (ALI) generating a nutrient gradient from lower media microchannel to the epidermis layer. Here, we have developed a human skin/skin cancer-on-a-chip platform in a perfused microfluidic device and evaluated the use of this device in assessing the efficacy of chemotherapeutics-loaded MNs for transdermal drug delivery applications (e.g., doxorubicin hydrochloride (DOX)) to treat skin cancer.

2. Experimental section

2.1. Cells and materials

Human dermal fibroblast cells (HDFs, PCS-201-012™), human epidermal keratinocyte cells (HEKs, PCS-200-011™), mus musculus skin melanoma cells (MCs, CRL-6475™), and human umbilical vein endothelial cells (HUVECs, PCS-100-010™) were purchased from ATCC. The three skin cells (HDFs, HEKs, and MCs) were cultured in their respective growth medium: keratinocyte growth medium 2 (KGM), melanocyte growth medium-M2 (MGM), and fibroblast growth medium (FGM), and HUVECs were cultured in endothelial cell growth medium 2 (EGM), all from PromoCell. HUVECs were used to model the vascular layer in our full-thickness skin model due to their proven ability to form capillary-like structures, which supports the vascularization process necessary for studying drug delivery and tissue interaction Although HUVECs were used in this study to form vascular networks, which are key for the functional integration of the skin model, we recognize that they are not typically found in the skin's dermis. Future developments of this model may involve the use of dermal microvascular endothelial cells (HDMECs) to better replicate the native skin vasculature. To support the co-culture of HEK, HDF, MC, and HUVEC cells, the media was optimized using a balanced co-culture medium of KGM:MGM (3:1), at the ALI to support HEKs differentiation and stratification into a fully differentiated epidermis, supplemented with 10 % FBS, 1 % penicillin-streptomycin, 2 mM L-glutamine, 0.4 μg/mL hydrocortisone, and 50 μg/mL ascorbic acid. This formulation was selected to meet the diverse requirements of the different cell types and maintain viability throughout the co-culture period. Type A porcine skin gelatin, methacrylic anhydride, photoinitiator (PI) (2-hydroxy-4-(2-hydroxyethoxyethoxy)-2-methypropiophenone), low viscosity alginic acid, formaldehyde solution (4 % v/v), Triton X-100, and bovine serum albumin were purchased from Sigma-Aldrich. Live/Dead cell viability kit (calcein acetoxymethyl/ethidium homodimer-1 (Calcein-AM/EthD-1), Alexa Fluor® 568 phalloidin, DAPI (4′,6-diamidino-2-phenylindole), Ki-67 antibody, Dulbecco's phosphate-buffered saline (DPBS; GIBCO), and stainless-steel catheter connectors (23G) were purchased from Thermo Fisher Scientific. Polydimethylsiloxane (PDMS; Sylgard) and DOX•HCl were purchased from Dow Corning and Oakwood Chemical, respectively. Tubing (Cole-Parmer Microbore Tubing, 0.020" × 0.060″OD) was purchased from Cole-Parmer.

2.2. Preparation of GelMA

High methacrylated gelatin was synthesized as described previously [50]. Briefly, 10 % w/v type A porcine skin gelatin in DPBS at 50 °C and under continuous stirring is added with methacrylic anhydride at 0.5 mL/min to reach the target volume. The resulting solution is allowed to react 1 h before 1:5 dilution with warm DPBS (40 °C) to stop the reaction. Further, dialysis against distilled water (12–14 kDa cut-off dialysis tubing) at 40 °C is performed to remove salts and methacrylic acid before lyophilizing and storage at −80 °C until further use. The GelMA hydrogels are prepared by diluting freeze-dried GelMA macromer in DPBS with 0.5 % w/v PI.

2.3. Preparation of vascular bioink and bioprinting procedure

Vascular bioink was prepared as described in our previous work

[43]. Briefly, GelMA macromer and alginate are dissolved in cell culture media with 0.5 % PI to a final concentration of 7.5 % GelMA and 2 % alginate. The resulting solution is filtration-sterilized with syringe filters (0.22 μm) and stored at 4 °C. The bioprinting was done using a BioX™ 3D Bioprinter (Cellink). Before use, GelMA/alginate bioink is warmed at 37 °C, and HUVEC cells are suspended at a final density of 8×10^6 cells/mL. Sterile UV-protected cartridges are loaded with vascular bioink and kept at 4 °C for 10 min for gelation before bioprinting. Bioprinting of vascular bioink is carried out according to the following parameters: printhead at 15 °C, printbed at 12 °C, applied pressure of 50–100 kPa, and linear printing speed of 2–6 mm/s. After the bioprinting process, the 3D structures are photo-crosslinked at 25 mW/cm^2 for 30 s.

2.4. Dermal layer

The dermal layer, comprising of GelMA (7.5 %) and PI (0.5 %) dissolved in cell culture media, and HDFs suspended at a density of 8×10^6 cells/mL is poured on the bioprinted vascular structures and crosslinked by UV exposure (25 mW/cm^2 for 3 min).

2.5. Generation of multilayered keratinocyte layers and epidermis maturation

The *in vitro* multilayered epidermis was obtained by multiple seeding steps. HEKs at 1×10^6 cells/mL are seeded on the GelMA layer and allowed to attach to the surface for 2 h, the media is then replaced by 1 % (w/v) porcine skin gelatin in growth media and incubated for 30 min to obtain a thin gelatin-coated layer, thus preparing the surface for a new HEKs seeding. Further, the skin tissues are cultured in a balanced co-culture medium of KGM:MGM (3:1) at the ALI to support HEKs differentiation and stratification into a fully differentiated epidermis.

2.6. Fabrication of microfluidic device and skin-on-a-chip model

The microfluidic device used to house the skin tissues is fabricated in PDMS through soft lithography. The aligned upper well and lower microchannel are separated by a TC-treated polyester membrane with 0.4 μm pores size. The upper and lower PDMS layers are prepared by molding PDMS prepolymer (10:1 ratio of PDMS and curing agent) on a microfabricated mold made of PMMA and curing the polymer at 75 °C for 4 h. After peeling the PDMS layers from the PMMA molds, the surface of the PDMS layer is treated with oxygen plasma (at 300 W for 2 min, 20 SCCM O_2 flow, and 0.65 mbar pressure) (Plasma Etch, Inc. PE-25). The plasma-treated surfaces are then immediately bonded. To control the flow of the culture medium, tubes are connected from the fluid medium and pump sources to the lower microfluidic channel using stainless steel catheter connectors. After sterilization of the PDMS devices by ethanol 70 % for 2 h and UV light exposure for 30 min, the endothelial layer is bioprinted on the polyester porous membrane at a density of 8×10^6 cells/mL and immediately photo-crosslinked at 25 mW/cm^2 for 30 s to prevent the GelMA hydrogels from mixing. The HDFs in GelMA at a density of 8×10^6 cells/mL are poured on the bioprinted structure and photo-crosslinked at the same conditions for 3 min. The multilayered HEKs layer is obtained by multiple seeding steps as described above. After 24 h of incubation, to start an air-liquid interface, the media from the top chamber is removed and the media flow in the lower microchannel is activated (5 μL/min).

2.7. Preparation of drug-loaded GelMA MNs

DOX-loaded GelMA MNs were prepared as described previously by Luo et al. [48]. Briefly, for the preparation of DOX-loaded GelMA MNs, 5.5 mg/mL of PI in DPBS and varying amounts of DOX in distilled water (1, 2, and 3 mg/mL) were mixed at 9:1 v/v ratio to make a final concentration of 5 mg/mL for PI and 100, 200, and 300 μg/mL for DOX. Then 200 mg of a commercially available GelMA (X-Pure GelMA 160P80 RG, Rousselot, France) was dissolved in 1 mL of the PI/DOX mixture. We chose to use X-Pure GelMA for fabricating our MNs to enhance their mechanical properties. The GelMA-DOX solution was added onto the PDMS MN molds (10 × 10H800 B200 P500, Micropoint Technologies, Singapore), followed by centrifugation at 3000 rpm (Centrifuge 5810, Eppendorf, Germany) for 2 min. The GelMA-DOX solution with the PDMS mold was irradiated with 365 nm UV light at 500 mW/cm^2 (SW0365A-25D, Orca Science, South Korea) for 30, 60, and 180 s. The resulting MNs with PDMS molds were protected from light, dried in a fume hood overnight at room temperature, and manually removed from the molds.

2.8. Fluorescence microscopy of DOX-loaded GelMA MNs

The DOX loading and shape of the DOX-loaded GelMA MNs were analyzed with a fluorescence microscope (Axio Observer, Zeiss, Germany).

2.9. Mechanical strength test of MNs

Mechanical testing of the MNs was performed using a 5943 Microtester Instron with a stress-strain gauge. The MNs were fixed on a stainless-steel plate with the needles pointing upward. The maximum loading force was set to 55 N and the stainless-steel plate was moved downward at a constant speed of 0.5 mm min^{-1}. The load (N) according to the displacement (mm) was plotted and the compressive load at the breakage point was measured.

2.10. In vitro release of DOX

The *in vitro* release of DOX from the MNs was evaluated by immersing MNs patches in 3 mL of DPBS containing 2 U mL^{-1} type II collagenase (Fisher Scientific, USA) at 37 °C. At predetermined timepoints, 100 μL of the sample was withdrawn for fluorescence (excitation: 480 nm, emission: 560 nm) measurement with a microplate reader (Varioskan LUX Microplate Reader, Thermo Fisher Scientific, USA) and returned to the whole sample.

2.11. Immunofluorescence assay

A Live/Dead Cell Viability Kit was employed to obtain cell viability. For 568 phalloidin (F-actin stain), DAPI (DNA stain), Ki-67 (antigen KI-67 stain), a-SMA (Alpha Smooth Muscle Actin stain), PCK (pan Cytokeratin stain), Filaggrin, Keratin 10, 14, and 19, Collagen I, and Fibronectin staining, *in vitro* skin tissues were fixed on days 1, 4, and 7. Cells were stained with 568 phalloidin at 1:200 dilution for 45 min, DAPI at 1:1000 dilution for 10 min, and for Ki-67, a-SMA, PCK, Filaggrin, Keratin 10, 14, and 19, Collagen I, and Fibronectin at 1:250 dilution in DPBS for 60 min in a humidity chamber, followed by washing three times with DPBS. Immunofluorescence microscopy was performed using an inverted fluorescence microscope (Zeiss Axio Observer 5 microscope) or a confocal microscope (BC LSM880).

2.12. Microscopy data analysis

ImageJ software was used for analysis of immunofluorescence images. The total number of cells or fluorescence intensity, according to experiment setup, were assessed for at least 3 replicates of each condition by using ImageJ. Similarly, the % of positive cells (at least 3 replicates) was obtained by counting cell nuclei stained by DAPI (total cell number) in the presence of specific protein stain with thresholds after subtracting backgrounds by using ImageJ.

2.13. Statistical analysis

In all experiments, a minimum of 3–5 chips per condition for both the skin model fabrication and the DOX dose experiment via MN application were evaluated. This sample size was chosen to ensure reliable and reproducible data across all conditions. At least three different samples were imaged to obtain the average values and standard deviation (s.d.) unless otherwise specified. One-way ANOVA comparisons tests were achieved in all statistical analyses. Statistics with a value of $P < 0.05$ were considered significant.

3. Results and discussions

Microneedling, a minimally invasive therapeutic technique, is a relatively new treatment option in dermatology [51,52]. This technique has been employed for many applications such as skin rejuvenation, scars, and drug delivery [45–47]. With the growing interest of MNs in precision medicine applications, a physiologically relevant skin model mimicking the *in vivo* structures and size is required to predict response to MNs while minimizing the use of animals. To demonstrate the developed skin-on-a-chip model and confirm its usefulness in skin disease modeling and physical therapy applications including microneedling, it was proposed to apply MNs for drug delivery against skin melanoma cells. Unlike previous skin models based on 2D and simple 3D cultures which have difficulties in testing transdermal drug delivery using MNs, the developed skin-on-a-chip model in this study can be an excellent substitution for real skin tissue with a thickness suitable for microneedling application and monitoring. To demonstrate this, a skin cancer model was established using the platform of skin-on-a-chip, and drug-loaded MNs were applied to target the melanoma cells.

3.1. Skin-on-a-chip setup and strategy to treat skin cancer

The skin provides a unique microenvironment where cells in different layers can interact, and gradients of nutrients from internal vascular networks with perfusion contribute to the functional specification of each skin layer. To explore the development and progression of skin-related diseases and assess the efficacy of drug treatments, a simple, time-efficient, robust, reliable, and scalable skin-on-a-chip platform of physiologically relevant skin structures was developed (Fig. 1A). The skin model was designed to work in an on-chip device fabricated with a PDMS microchannel for perfusion of media, a porous polyester membrane (0.4 μm pores), and a PDMS skin chamber; all components were assembled via oxygen plasma bonding (Fig. 1B and C). The porous membrane separated the upper chamber containing skin layers and the lower media microchannel. The physiologically relevant skin model was fabricated by a combination of: (1) bioprinted endothelial cells (ECs) in GelMA-alginate bioink on the porous membrane, allowing HDFs-ECs interactions and facilitating the diffusion of media, (2) a 3D dermis equivalent constructed by encapsulating HDFs in GelMA hydrogels, and (3) a stratified, fully differentiated epidermis obtained on the dermis layer by seeding HEKs multiple times with gelatin coating to shorten the incubation time and maturating the *in vitro* tissue. After a certain period, the media in the upper skin chamber is removed, and the media flow in the lower microchannel is activated to create an ALI (Fig. 1D), which generates a nutrient gradient from the lower media microchannel to the epidermis layer, aiding HEKs differentiation and maturation into a stratified epidermis. Furthermore, this multifunctional platform was used to create a human skin cancer model and to test targeting the cancer cells through transdermal drug delivery using MNs loaded with chemotherapy drugs (i.e., DOX) (Fig. 1E).

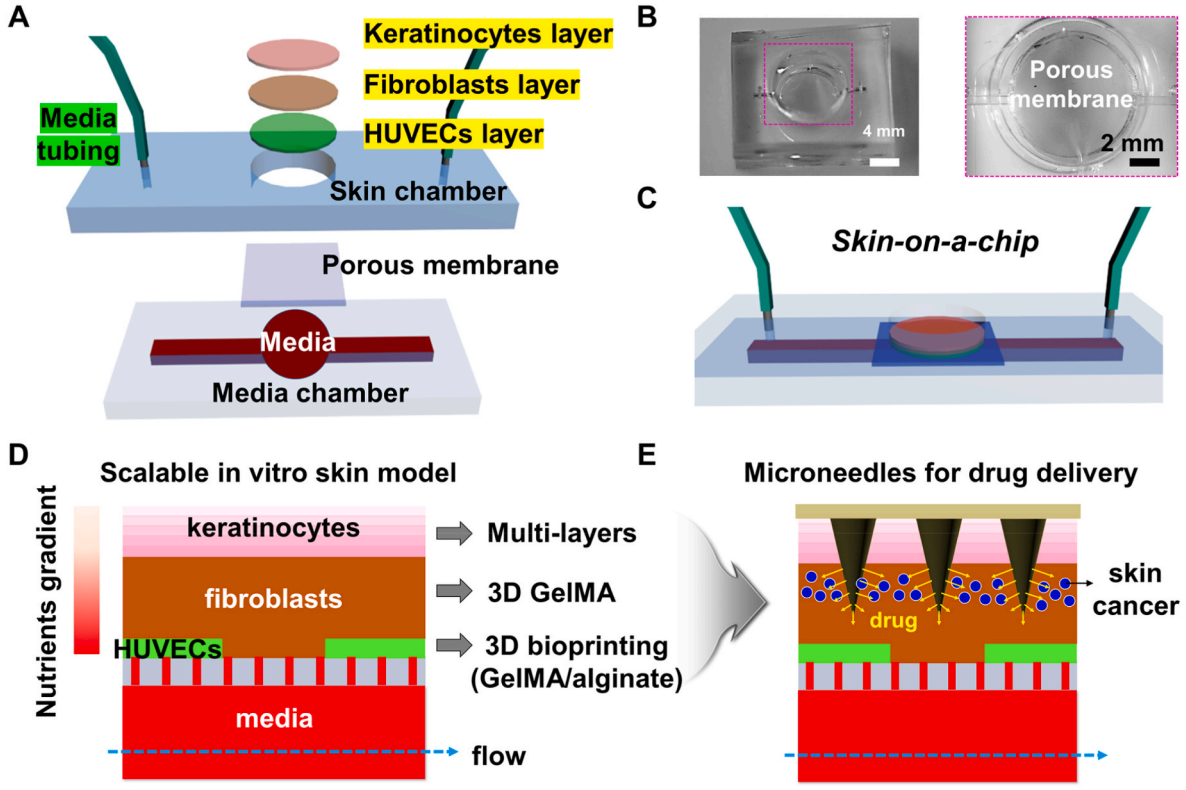

Fig. 1. Skin-on-a-chip setup and strategy with a thickness suitable for microneedling application and monitoring. (A) Schematic diagram of the 3D Skin-on-a-chip model set-up. (B) Photograph of a PDMS chip and porous membrane between skin and media chambers. (C) Schematic representation of the assembled skin-on-a-chip system. (D) Schematic showing the cross-sectional structure of the proposed skin model-on-a-chip platform. (E) Schematic showing the application of MNs for transdermal drug delivery to cancer cells in the skin cancer model-on-a-chip.

3.2. Air-liquid interface culture for epidermal layers and cellular morphology characteristics

In this study, we biofabricated a 3D *in vitro* skin model to recapitulate the epidermal and dermal layers, crucial for mimicking the structure and function of native skin. HDFs were encapsulated within GelMA to compose the dermis layer on day 0, followed by the seeding of HEKs on the surface of the dermis layer on day 7. The transition from submerged culture to ALI on day 14 was intended to induce keratinocyte differentiation, fostering the formation of a stratified epidermal layer (Fig. 2A and B).

Confocal microscopy coupled with immunofluorescence staining was utilized to assess cellular organization and marker expression over time. We observed a significant increase in cell density between days 10 and

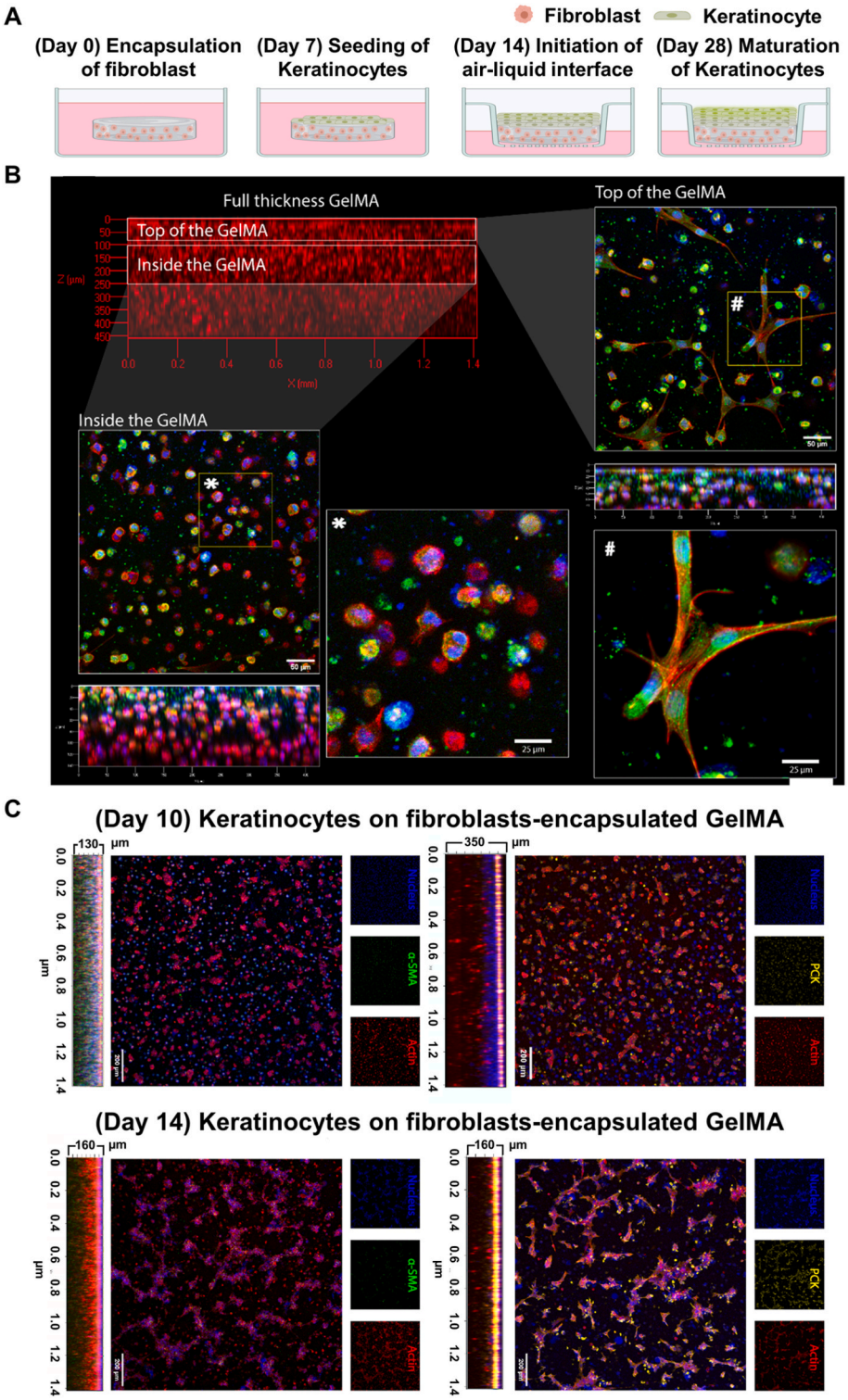

Fig. 2. Air-liquid interface culture for epidermal layers and cellular morphology characteristics. (A) Schematic diagram of ALI culture method for cultivating and differentiating keratinocytes to form a stratified epidermis. Representative confocal images of (B) the 3D dermal layer and (C) the epidermal layers on days 10 and 14. Blue: Nucleus; Red: Actin; Green: α-SMA; Yellow: Pan-cytokeratin.

14, as indicated by the increase in nuclear and actin staining across the matrix (Fig. 2C). The proliferation suggests an active cellular environment within the epidermal and dermal compartments of the model.

The differentiation and identity of fibroblasts and keratinocytes were specifically monitored using alpha-smooth muscle actin (a-SMA) and pan-cytokeratin (PCK) markers, respectively. a-SMA is a well-established marker for fibroblasts, particularly those transitioning towards a myofibroblast phenotype, which plays a pivotal role in extracellular matrix remodeling and wound healing. The consistent expression of a-SMA across the dermal layer indicates the maintenance of a fibroblast-rich environment within the model. PCK, a pan-cytokeratin marker, was employed to identify keratinocytes, the primary cell type of the epidermis. The increase in PCK signal from day 10 to day 14 highlights the differentiation and proliferation of keratinocytes, critical steps in epidermal layer formation. The observed data suggest that the ALI culture effectively promotes the development of a stratified epidermis, akin to native skin architecture.

While the initial characterization using a-SMA and PCK provided valuable insights into fibroblast and keratinocyte dynamics within the model, further marker analysis would enhance the characterization of

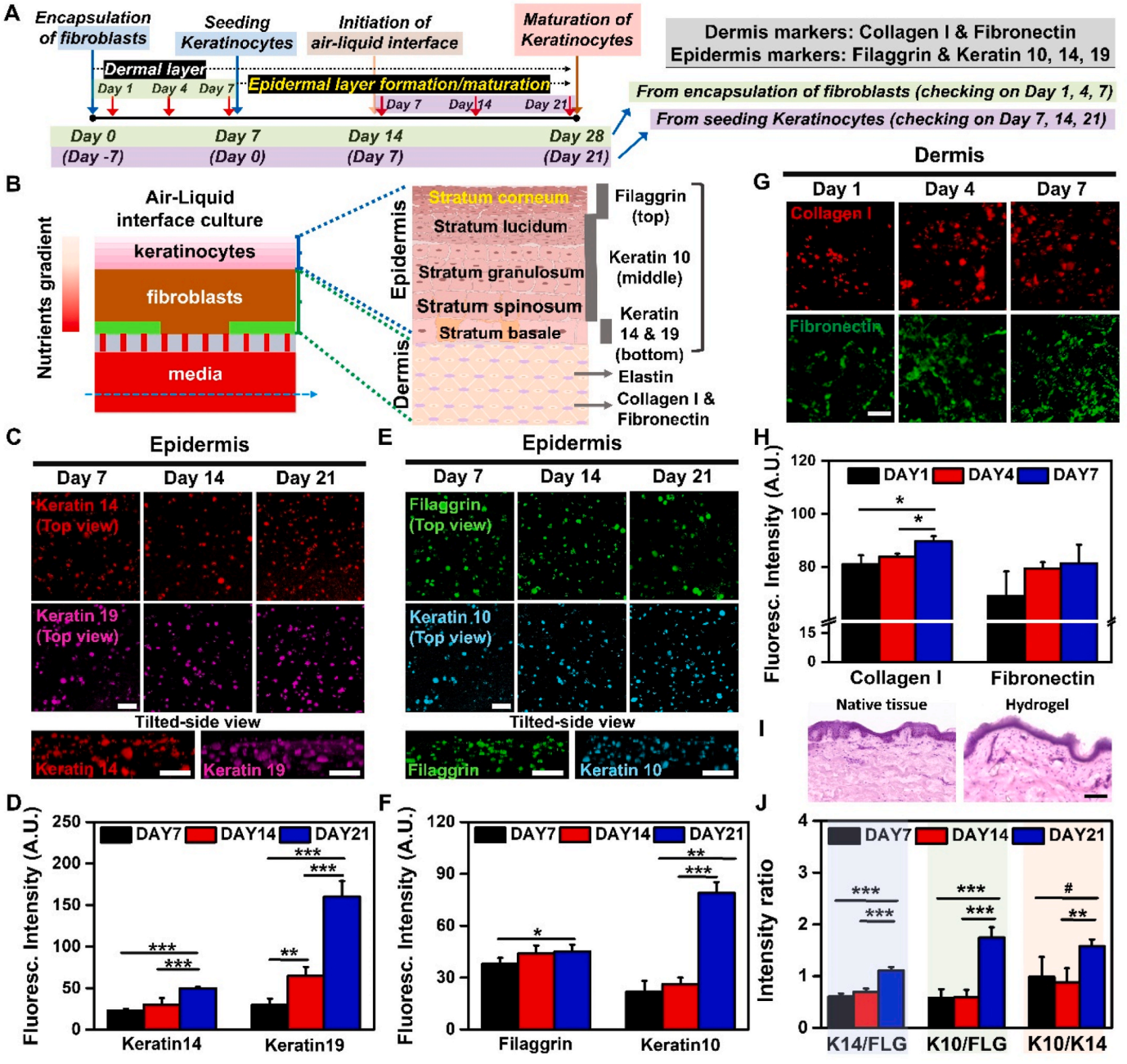

Fig. 3. Characteristics of dermal and epidermal layers with representative marker expression. (A) Timepoint of multi-layered skin model-on-a-chip formation based on dermal layer and epidermal layer fabrication: two different timepoints. (B) Characteristics of marker expression at different depths of epidermal and dermal layers. Representative confocal images and fluorescence intensities of (C and D) Filaggrin and Keratin 14 (epidermis markers), (E and F) Keratin 19 and 10 (epidermis markers), and (G and H) Collagen I and Fibronectin (dermis markers). I) Hematoxylin and eosin (H&E) staining of native human skin with stratified, cornified epidermis and papillary and reticular dermis and *in vitro* skin tissue biofabricated in hydrogel. Scale bars: 100 μm. (J) Relative ratio of marker expression changes across different layers of the epidermis (FLG: Filaggrin_Stratum corneum marker, K14: Keratin 14_Stratum basale marker, K10: Keratin 10_Stratum lucidum to spinosum marker).

the *in vitro* skin model. Markers such as Filaggrin, Keratin 14, Keratin 19, and Keratin 10 would offer deeper insights into keratinocyte differentiation states and stratification. Additionally, evaluating extracellular matrix components like Collagen I and Fibronectin would elucidate the structural integrity and matrix remodeling within the dermal layer. While a-SMA was used in this study to identify fibroblasts within the co-cultures and assess fibroblast activation, we acknowledge the importance of vimentin as a general marker for fibroblasts. Future studies will consider incorporating vimentin to provide a more comprehensive characterization of fibroblast phenotypes in our full-thickness skin model, ensuring a clearer distinction between activated fibroblasts and myofibroblasts.

3.3. Characteristics of dermal and epidermal layers with representative marker expression

Our model was fabricated according to the following timeline. First, a dermal layer with fibroblasts was printed and cultured for 7 days. On day 7 of the dermal layer, an epidermal layer with keratinocytes was fabricated and cultured for 21 days (28 days of total culture for fibroblasts). Dermal layer samples on days 1, 4, and 7, were stained for collagen I and fibronectin. Epidermal layer samples on days 7, 14, and 21, were stained for filaggrin (FLG), keratin 10 (K10), keratin 14 (K14), and keratin 19 (K19) (Fig. 3A). The epidermis of the skin is composed of several distinct layers, each with specific functions and characteristics: the stratum basale, stratum spinosum, stratum granulosum, stratum lucidum, and stratum corneum (from bottom to top) (Fig. 3B). The stratum basale, located at the deepest layer, can indicate the activation and differentiation of basal layer cells through the expression of K14 and K19. The intermediate layers (stratum spinosum, stratum granulosum, and stratum lucidum) contribute to forming the skin's protective barrier through cell maturation and functional changes, which can be confirmed through the expression of K10. The outermost layer, the stratum corneum, is a cornified layer composed of dead keratinocytes that have undergone terminal differentiation, which can be confirmed by the expression of FLG [50,53,54].

To evaluate the maturation and cornification of the epidermal layer, we conducted immunofluorescence staining of K10, K14, K19, and FLG for keratinocytes cultured on days 7, 14, and 21. Expression levels of K14 and K19 for cells in the basal layer of the epidermis increased over time (~2.17 and ~5.4-fold changes between day 1 and day 7, respectively) (Fig. 3C and D). Similarly, keratinocytes showed increased levels of FLG in the terminal stratum corneum and K10 expression in the stratum granulosum increased over time (~1.18 and ~3.6-fold changes between day 1 and day 7, respectively) (Fig. 3E and F). The elevated expression of FLG indicates that the cornification process is progressing effectively [55]. It is well known that collagen I, primarily produced by fibroblasts, is a key component of the extracellular matrix (ECM) that provides the dermis with its physical strength and elasticity [56]. In addition, fibronectin binds to integrins on the cell surface to facilitate cell adhesion and interacts with collagen, elastin, and proteoglycans, forming a complex network in ECM [57–59].

To determine whether our dermal model is functioning properly in terms of physiological similarity and the ability to maintain cellular function compared to the native tissue, immunofluorescence staining of collagen I and fibronectin was performed. The expression levels of collagen I and fibronectin increased in the dermal layers from day 1 to day 7, although it was not significantly increased (~1.18 and ~1.11-fold changes between day 1 and day 7, respectively) (Fig. 3G and H). These results indicate that the synthesized ECM components effectively mimic the function of native dermal tissues, suggesting that ECM formation and tissue maturation have progressed over time [60,61]. Additionally, the increased levels of fibronectin expression could induce collagen contraction and contribute to ECM remodeling and wound closure [62].

To simultaneously evaluate the differentiation and activation of cells, we analyzed the expression ratios of specific markers (K14/FLG, K10/FLG, K10/K14) at the different epidermis layers. On day 21, the K14/FLG and K10/FLG ratios were 1.10 and 1.74, respectively, showing that the increase in FLG marker expression levels was much less compared to the increase in K10. This suggests that hyperplastic epidermis might not occur. Additionally, the increase in the K14/FLG and K10/FLG ratios on day 21 indicates that the activation of basal and granular layer cells may be more prominent compared to the degree of cornification on day 7 (Fig. 3J). We acknowledge that it may not visually appear as a fully stratified epidermis layer in the current fluorescence images. Nevertheless, our data, including markers for KC differentiation, indicate that the cells undergo the necessary processes to form a multilayered structure over time, mimicking the natural stratification of the epidermis and contributing to the formation of the epidermal layer.

The hematoxylin and Eosin (H&E) staining results demonstrate that the *in vitro* skin tissue closely resembles the structure and organization of native skin (Fig. 3I). The histological images reveal distinct epidermal and dermal layers, with organized keratinocyte layers in the epidermis and a densely populated dermal region containing fibroblast cells. Similar to findings reported in previous studies, our model replicates essential structural elements of native skin, supporting a layered, stratified epidermis with differentiated basal, spinous, and granular cell layers that mirror native tissue architecture [63–65]. This formation is indicative of a functional skin barrier, which is a crucial aspect of effective *in vitro* models and their application in drug testing and skin research.

Moreover, the dermal layer's composition, with fibroblasts dispersed within a matrix that mimics the extracellular environment, aligns with observations from other advanced skin models, which emphasize the importance of fibroblast-seeded dermal layers for producing collagen and promoting tissue stability [66–68]. This similarity to native skin tissue suggests that our *in vitro* model effectively mimics the physiological conditions of native ECMs in the skin, offering a robust platform for simulating skin physiology and demonstrating high levels of epidermal maturation and differentiation. Such features enhance the relevance of our skin model for applications in drug delivery, biomaterial testing, and cosmetics.

3.4. Skin cancer-on-a-chip setup and highly metastatic melanoma

The development of *in vitro* skin cancer models is crucial for advancing our understanding of cancer biology and improving therapeutic strategies. These models provide a controlled environment to study tumor behavior, interactions with surrounding tissues, and the effectiveness of potential treatments. Specifically, melanoma is one of the deadliest forms of skin cancer, and creating accurate models that mimic its tumorigenic and metastatic properties is vital for preclinical research.

B16F10 murine melanoma cells (MCs) are extensively used as a skin cancer model due to their high tumorigenic and metastatic capabilities [69]. In this study, a layer of MCs was embedded approximately 400 μm below the epidermis surface, within the dermis layer (Fig. 4A). Before assessing the effectiveness of localized drug delivery using DOX-loaded GelMA MNs, the viability of cells within the skin cancer model was evaluated (Fig. 4B). Notably, it was observed that the nutrient gradient from the internal vascular networks, enhanced by perfusion, significantly promoted the invasion of MCs (labeled with a blue cell tracker CellTracker™ Blue CMAC) toward the media flow in the lower microchannel (Fig. 4C). Additionally, under the ALI, a considerable number of both live and dead HEKs were present in the epidermis layer, while the viability of HDFs and MCs in the dermis layer remained largely unaffected.

3.5. Characteristics of DOX-loaded MNs and transdermal microneedling test targeting melanoma region

For delivering anti-cancer drugs to the skin cancer model, a GelMA

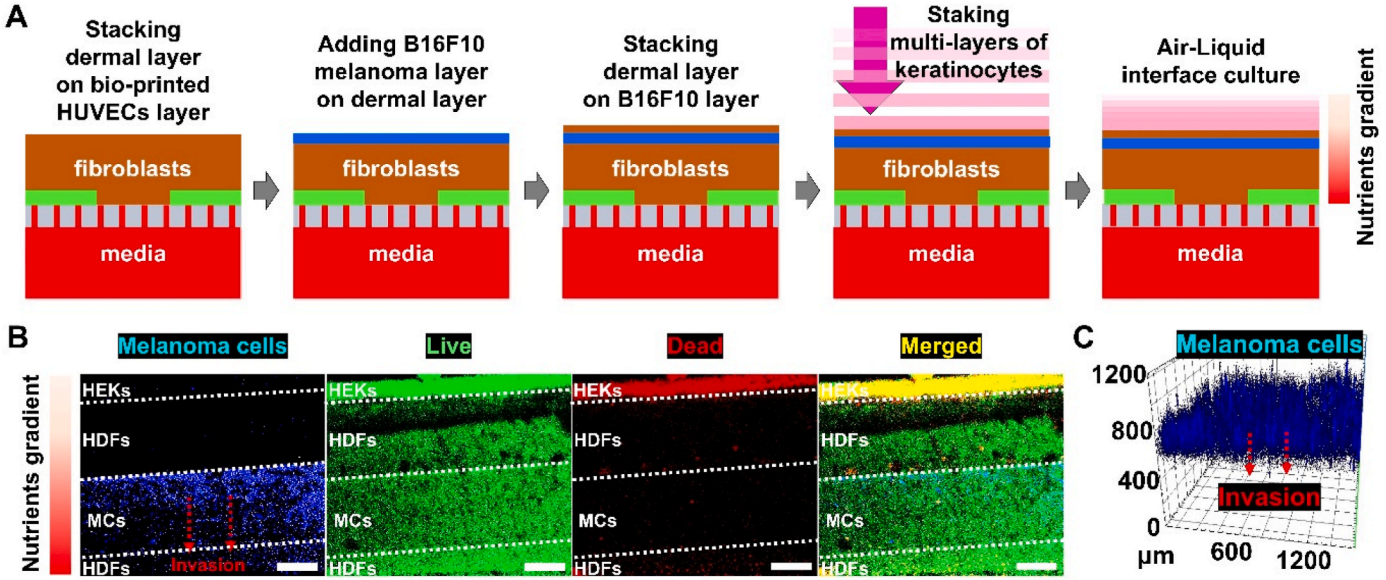

Fig. 4. Skin cancer-on-a-chip setup and highly metastatic melanoma. (A) Schematic diagram of skin cancer model-on-a-chip fabrication: addition of a skin cancer layer in the dermal layer. (B) Representative cross-sectional live/dead images of the 3D skin cancer model-on-a-chip after 24 h of ALI culturing. Invasion of melanoma cells (blue) directed to the media microchannel direction was observed. Scale bars: 200 μm. C) Representative 3D image from MCs within the 3D *in vitro* skin model.

MN patch was prepared as previously reported by Luo et al. [70]. Briefly, GelMA prepolymer solutions containing DOX were filled into a MN mold and crosslinked by UV radiation before solidification by drying at room temperature. The MNs with sharp tips (200 × 200 μm base, 500 μm spacing, and 800 μm height) were uniform in shape and size and homogenously loaded with DOX as shown with fluorescence imaging of DOX (Fig. 5A).

To optimize the crosslinking time for MN fabrication, the mechanical strength against compression was measured for each MN of different crosslinking times (30, 60, and 180 s) (Fig. 5B). The slope of the displacement-load curve (compressive modulus/cross-sectional area) increased as the crosslinking time increased (Fig. 5C). The release profiles of DOX-loaded GelMA MNs displayed a similar tendency in time-dependent release and MNs with higher drug amounts showed a higher amount of DOX release (Fig. 5D).

To prove that MNs could penetrate the proposed skin model and reach the embedded skin cancer cell layer, the insertion of drug-free GelMA MNs was monitored with blue tracker-labeled MCs (Fig. 5E). Microindentation including uneven surfaces, and a puncture caused by MNs in the cancer layer were observed (Fig. 5F). Then, DOX-loaded MNs were patched to the skin cancer model. Uniform penetration of MNs into the model at ~600 μm depth was observed, indicating that the MNs can reach the MC layer for localized drug delivery (Fig. 5G). We employed the MN technique because there is no *in vitro* skin model to demonstrate the possibility of drug delivery to localized cancer cells using MNs. We embedded the MCs in the dermis layer (in a depth of ~0.5 mm from the surface) because in general epidermis layer thickness of human skin ranges from ~0.5 mm (thinnest, like eyelids) to ~1.5 mm (thickest). Since MCs located in epidermis layers are known to invade through the papillary dermis, we tried to target invading MCs using drug-loaded MNs in this study.

3.6. Transdermal drug delivery via MNs to localized cancer cells

To evaluate the efficacy of microneedling for skin cancer treatment, three conditions were tested in our melanoma skin model (Fig. 6). In condition (A), DOX was introduced through the media channel at a concentration of 3.33 μg/mL (in a total of 3 mL) for 24 h to mimic systemic administration levels. This concentration aligns with a localized treatment approach while remaining lower than typical blood concentrations seen after intravenous infusion (approximately 22.95 μg/mL) [71]. Cell death induced by DOX was visualized with EthD-1 staining, revealing a gradient of cell death from the lower microchannel to the upper skin layers. This resulted in minimal MC death, indicating that systemic-like delivery through media channels has limited efficacy in targeting the MCs directly.

Next, MNs were tested under two conditions: (B) as a control (DOX-free MNs) and (C) with DOX-loaded MNs at a loading of 300 μg/mL GelMA, equivalent to a controlled release of approximately 10 μg of DOX (or 3.33 μg/mL in the system containing 3 mL of media). The MNs were inserted for 24 h before removal, and EthD-1 staining showed significant cell death localized to MCs in the epidermal layer when DOX-loaded MNs were used. In contrast, DOX-free MNs caused minimal cell death, highlighting the advantage of DOX delivery via MNs. The localized effect of DOX-loaded MNs produced a clear radial pattern of cell death emanating from each needle site, effectively concentrating cytotoxic effects on MCs. Consequently, this targeting approach with MNs offers more efficient tumor cell death than traditional systemic-like delivery through the media channel. This reinforces the potential of MNs as a precise, localized delivery system for skin cancer treatment, as shown in Fig. 6A–C.

These results using the proposed reliable and scalable skin-on-a-chip platform are comparable to outcomes from *in vivo* animal studies using MN techniques [72,73]. Furthermore, the skin-on-a-chip platform in this study may apply to *in vitro* skin models (with/without diseases) for various therapeutic or cosmetic developments and may eventually replace an animal model. To further expand and validate the current model compared to animal model, future investigations incorporating important components in native skin tissues, such as hypodermis, appendages, pigmentation, sweat glands, immune cells, and various mechanical signals that control tumor development and function may be required. With these more complicated functionalities and structures of the skin, a better model recapitulating the native behaviors of skin tissues for realizing personalized medicine could be achieved. To demonstrate the multifunctionality of our proposed model, we developed a skin cancer model that shows how MNs can deliver drugs directly to localized cancer cells.

This study focuses on the development and validation of a full-

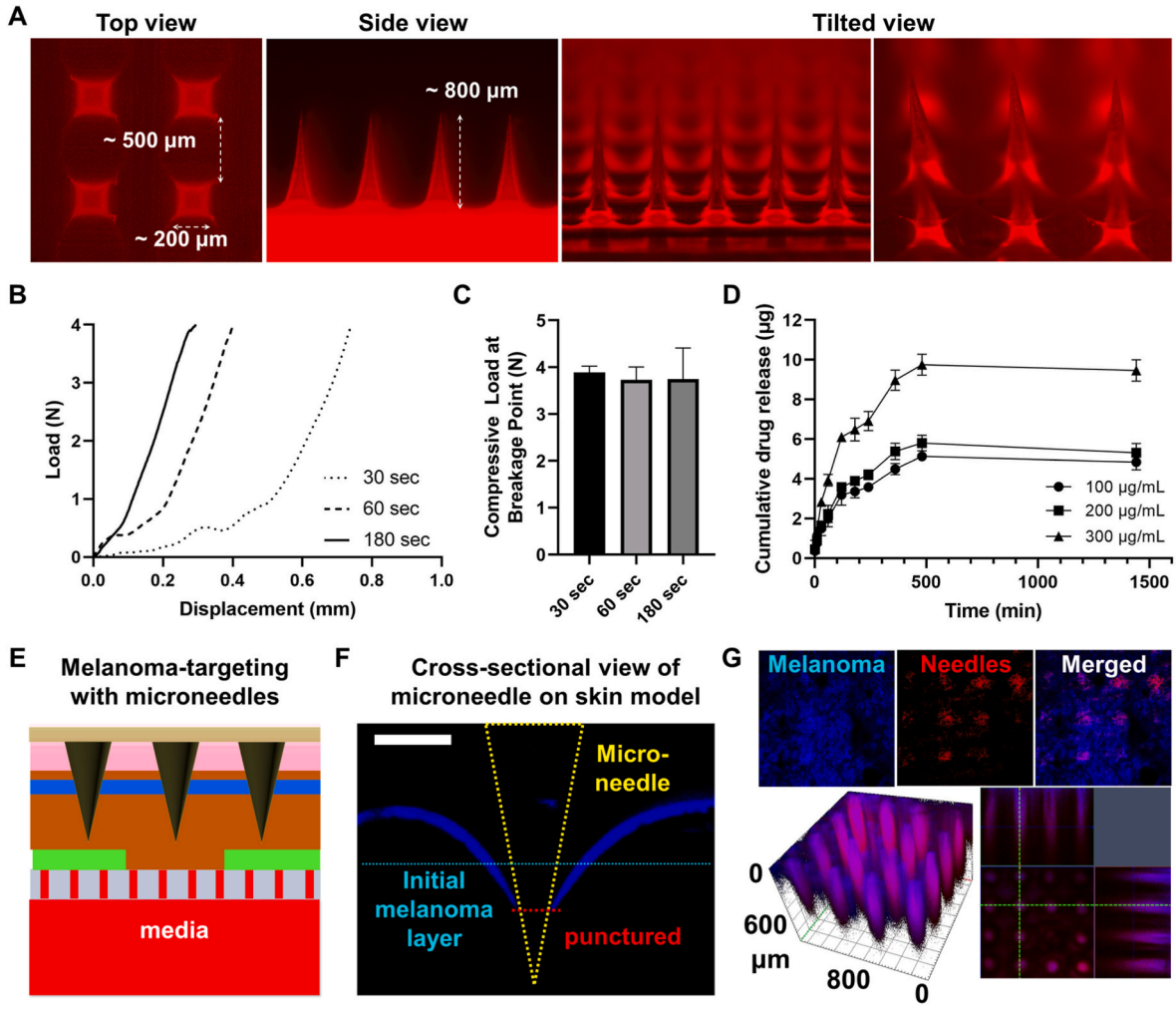

Fig. 5. Characteristics of DOX-loaded MNs and transdermal microneedling test targeting melanoma region. (A) Representative images of DOX-loaded GelMA MNs, tilted view, side view, and 3D construction from multi-confocal imaging. (B) Stress-strain curve, (C) Compressive moduli of MNs photo-crosslinked at 30, 60, and 180 s. (D) Cumulative drug release of MNs loaded with different amounts of DOX (100, 200, and 300 µg/mL). (E) Schematic diagram of 3D Skin cancer-on-a-chip fabrication and DOX-loaded GelMA MN patch application. A representative cross-sectional confocal image of the 3D skin cancer model with inserted (F) single needle and (G) array of MNs, note that the layer of melanoma cells has been reached and punctured. Scale bars: 200 µm.

thickness skin-on-a-chip platform, designed to simulate human skin for therapeutic testing. The application of DOX-loaded MNs is included as a proof-of-concept to showcase the model's versatility in evaluating drug delivery systems. While exploring microneedle-mediated dermal effects is beyond the scope of this manuscript, the microneedle experiments highlight the potential of this platform for future investigations. However, MN-mediated drug delivery has been extensively studied in prior research, which reports minimal dermal damage under optimized conditions. For instance, a previous review demonstrated that MNs achieve localized drug delivery with negligible disruption to surrounding cells [74]. Similarly, careful control of MN depth and spacing minimizes dermal cell death while ensuring therapeutic efficacy [48,75]. These findings provide a strong basis for the assumption that microneedle application in our system would cause minimal disruption to dermal tissues under optimized conditions. Nevertheless, future studies should include quantitative assessments of dermal cell viability, such as live/-dead assays and apoptosis marker evaluations, to further elucidate the safety of microneedle-mediated drug delivery. These evaluations would provide additional insights into the potential side effects and optimize the design of microneedles for broader therapeutic applications.

4. Conclusion

Our study successfully developed and applied a skin/skin cancer model-on-a-chip platform that closely mimics *in vivo* skin structures and functions through advanced bioprinting and bioengineering techniques. This platform enabled the creation of vascular, dermal, and epidermal layers, and the establishment of a melanoma model within the dermal layer. Our findings demonstrated that drug delivery using chemotherapeutic-loaded MNs significantly enhances targeting precision and treatment efficacy for skin cancer compared to traditional bloodstream-based methods. This innovative model offers a robust and scalable alternative to animal models, providing a reliable tool for studying disease mechanisms and evaluating therapeutic interventions, with potential applications in both medical and cosmetic fields. Future research should focus on integrating additional native skin components and mechanical signals to improve the model's relevance and functionality, ultimately advancing personalized medicine.

CRediT authorship contribution statement

Natan R. Barros: Writing – original draft, Visualization, Validation, Investigation, Formal analysis, Data curation, Conceptualization. **Raehui Kang:** Writing – original draft, Visualization, Investigation, Formal

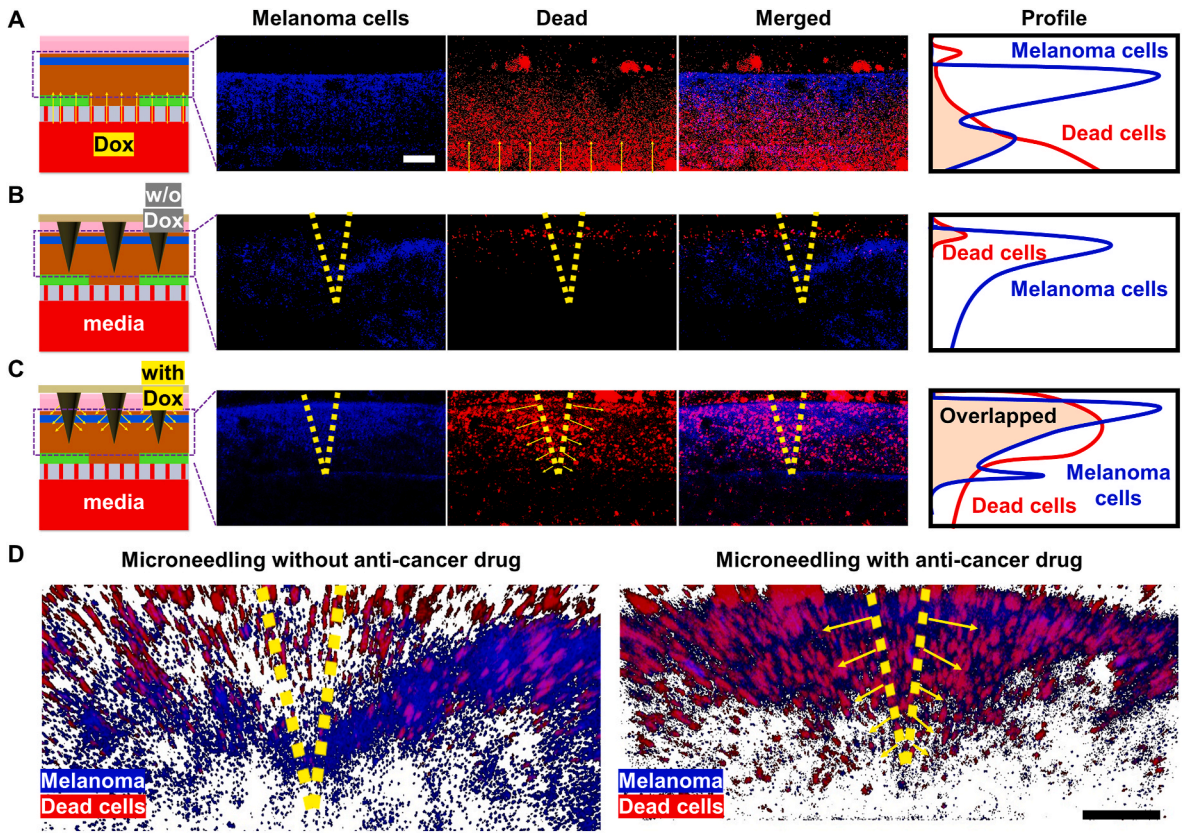

Fig. 6. Transdermal drug delivery via MNs to localized cancer cells. Representative cross-sectional confocal images of skin cancer model-on-a-chip. (A) DOX perfused through the media microchannel (3.33 μg/mL in a total of 3 mL), (B) Dox-free GelMA MNs (as a control) punctured on the 3D skin cancer model, (C) DOX-loaded GelMA MNs punctured on the 3D skin cancer model. Profiles of melanoma and dead cells from cross-sectional images, verifying the efficiency of transdermal drug delivery via MNs when compared with overlapped regions. (D) Representative z-stacked cross-sectional images of melanoma layers in the dermis layer without or with DOX, (left) DOX-free GelMA MNs, (right) DOX-loaded GelMA MNs. Scale bars: 200 μm.

analysis, Data curation, Conceptualization. **Jinjoo Kim:** Writing – original draft, Visualization, Validation, Investigation, Formal analysis, Data curation. **Menekse Ermis:** Investigation, Formal analysis, Data curation. **Han-Jun Kim:** Validation, Investigation, Formal analysis, Data curation, Conceptualization. **Mehmet R. Dokmeci:** Validation, Formal analysis, Conceptualization. **Junmin Lee:** Writing – review & editing, Writing – original draft, Visualization, Validation, Supervision, Project administration, Methodology, Funding acquisition, Formal analysis, Conceptualization.

Declaration of competing interest

The authors declare no competing interest.

Acknowledgements

Natan R. Barros and Raehui Kang equally contributed to this work. N. B. thanks the support of São Paulo Research Foundation – FAPESP program in Brazil – award no. (2018/11861–0). J.L acknowledges funding from National Research Foundation of Korea (NRF) grant (RS-2023-00211096, RS-2023-00260454, and RS-2024-00403376) funded by the Korean government (MSIT).

Data availability

Data will be made available on request.

References

[1] J. Powell, Skin physiology women's heal, Méd. 3 (2006) 130–133.
[2] N.H. Nicol, Anatomy and physiology of the skin, Dermatol. Nurs. 17 (2005) 62.
[3] M. Venus, J. Waterman, I. McNab, Basic Physiology of the Skin Surg, vol. 28, 2010, pp. 469–472.
[4] R.E. Pecoraro, J.H. Ahroni, E.J. Boyko, V.L. Stensel, Chronology and Determinants of Tissue Repair in Diabetic Lower-Extremity Ulcers Diabetes 40 (1991) 1305–1313.
[5] E. McLafferty, C. Hendry, F. Alistair, The integumentary system: anatomy, physiology and function of skin Nurs, STAND 27 (2012) 35–42.
[6] S.Y. Tan, Z. Leung, A.R. Wu, Recreating Physiological Environments In Vitro: Design Rules for Microfluidic-Based Vascularized Tissue Constructs Small 16 (2020) 1905055.
[7] N. Ashammakhi, S. Ahadian, C. Xu, H. Montazerian, H. Ko, R. Nasiri, N. Barros, A. Khademhosseini, Bioinks and bioprinting technologies to make heterogeneous and biomimetic tissue constructs Mater, Today Bio 1 (2019) 100008.
[8] K. Fetah, P. Tebon, M.J. Goudie, J. Eichenbaum, L. Ren, N. Barros, R. Nasiri, S. Ahadian, N. Ashammakhi, M.R. Dokmeci, A. Khademhosseini, The emergence of 3D bioprinting in organ-on-chip systems Prog, Biomed. Eng. 1 (2019) 012001.
[9] N. Ashammakhi, R. Nasiri, N.R. De Barros, P. Tebon, J. Thakor, M. Goudie, A. Shamloo, M.G. Martin, A. Khademhosseni, Gut-on-a-chip: Current progress and future opportunities Biomaterials (2020) 120196.
[10] S.N. Steinway, J. Saleh, B.-K. Koo, D. Delacour, D.-H. Kim, Human microphysiological models of intestinal tissue and gut microbiome, Front. Bioeng. Biotechnol. 8 (2020) 725.
[11] G.S. Offeddu, Y. Shin, R.D. Kamm, Microphysiological models of neurological disorders for drug development Curr, Opin. Biomed. Eng. 13 (2020) 119–126.
[12] C.S. Lee, K.W. Leong, Advances in microphysiological blood-brain barrier (BBB) models towards drug delivery, Curr. Opin. Biotechnol. 66 (2020) 78–87.
[13] X. Zhang, M. Bishawi, G. Zhang, V. Prasad, E. Salmon, J.J. Breithaupt, Q. Zhang, G. A. Truskey, Modeling early stage atherosclerosis in a primary human vascular microphysiological system, Nat. Commun. 11 (2020) 5426.
[14] N. Arumugasaamy, K.D. Rock, C.-Y. Kuo, T.L. Bale, J.P. Fisher, Microphysiological systems of the placental barrier, Adv. Drug Deliv. Rev. 161–162 (2020) 161–175.
[15] C.M. Sakolish, M.B. Esch, J.J. Hickman, M.L. Shuler, G.J. Mahler, Modeling Barrier Tissues in Vitro: Methods, Achievements, and Challenges EBioMedicine, vol. 5, 2016, pp. 30–39.
[16] M.J. Randall, A. Jüngel, M. Rimann, K. Wuertz-Kozak, Advances in the biofabrication of 3D skin in vitro: healthy and pathological models, Front. Bioeng. Biotechnol. 6 (2018) 154.

[17] M. Lee, J.-H. Hwang, K.-M. Lim, Alternatives to in vivo draize rabbit eye and skin irritation tests with a focus on 3D reconstructed human cornea-like epithelium and epidermis models, Toxicol. Res. 33 (2017) 191–203.

[18] F. Huet, M. Severino-Freire, J. Chéret, O. Gouin, J. Praneuf, O. Pierre, L. Misery, C. Le Gall-Ianotto, Reconstructed human epidermis for in vitro studies on atopic dermatitis, A review J. Dermatol. Sci. 89 (2018) 213–218.

[19] T. do N. Pedrosa, C.M. Catarino, P.C. Pennacchi, S R de Assis, F. Gimenes, M.E. L. Consolaro, S.B. de M. Barros, S.S. Maria-Engler, A new reconstructed human epidermis for in vitro skin irritation testing, Toxicol. Vitro 42 (2017) 31–37.

[20] C. Capallere, C. Plaza, C. Meyrignac, M. Arcioni, M. Brulas, V. Busuttil, I. Garcia, É. Bauza, J.-M. Botto, Property characterization of reconstructed human epidermis equivalents, and performance as a skin irritation model, Toxicol. Vitro 53 (2018) 45–56.

[21] H. Niehues, J.A. Bouwstra, A. El Ghalbzouri, J.M. Brandner, P.L.J.M. Zeeuwen, E. H. van den Bogaard, 3D skin models for 3R research: the potential of 3D reconstructed skin models to study skin barrier function, Exp. Dermatol. 27 (2018) 501–511.

[22] R. Hubaux, C. Bastin, M. Salmon, On the relevance of an in vitro reconstructed human epidermis model for drug screening in atopic dermatitis Exp, Dermatol 27 (2018) 1403–1407.

[23] C.M. Catarino, T. do Nascimento Pedrosa, P.C. Pennacchi, S.R. de Assis, F. Gimenes, M.E.L. Consolaro, S.B. de Moraes Barros, S.S. Maria-Engler, Skin corrosion test: a comparison between reconstructed human epidermis and full thickness skin models, Eur. J. Pharm. Biopharm. 125 (2018) 51–57.

[24] M. Bataillon, D. Lelièvre, A. Chapuis, F. Thillou, J.B. Autourde, S. Durand, N. Boyera, A.-S. Rigaudeau, I. Besné, C. Pellevoisin, Characterization of a new reconstructed full thickness skin model, T-Skin^{TM}, and its application for investigations of anti-aging compounds, Int. J. Mol. Sci. 20 (2019) 2240.

[25] S. Girardeau-Hubert, C. Deneuville, H. Pageon, K. Abed, C. Tacheau, N. Cavusoglu, M. Donovan, D. Bernard, D. Asselineau, Reconstructed skin models revealed unexpected differences in epidermal african and caucasian skin, Sci. Rep. 9 (2019) 7456.

[26] A. Berroth, J. Kühnl, N. Kurschat, A. Schwarz, F. Stäb, T. Schwarz, H. Wenck, R. Fölster-Holst, G. Neufang, Role of fibroblasts in the pathogenesis of atopic dermatitis, J. Allergy Clin. Immunol. 131 (2013) 1547–1554.e6.

[27] A. Cochrane, H.J. Albers, R. Passier, C.L. Mummery, A. van den Berg, V.V. Orlova, A.D. van der Meer, Advanced in vitro models of vascular biology: human induced pluripotent stem cells and organ-on-chip technology, Adv. Drug Deliv. Rev. 140 (2019) 68–77.

[28] Q. Wu, J. Liu, X. Wang, L. Feng, J. Wu, X. Zhu, W. Wen, X. Gong, Organ-on-a-chip: recent breakthroughs and future prospects, Biomed. Eng. Online 19 (2020) 9.

[29] J.E. Sosa-Hernández, A.M. Villalba-Rodríguez, K.D. Romero-Castillo, M.A. Aguilar-Aguila-Isaías, I.E. García-Reyes, A. Hernández-Antonio, I. Ahmed, A. Sharma, R. Parra-Saldívar, H.M.N. Iqbal, Organs-on-a-Chip Module: A Review from the Development and Applications Perspective Micromachines, vol. 9, 2018, p. 536.

[30] Q. Ramadan, M. Zourob, Organ-on-a-chip engineering: toward bridging the gap between lab and industry, Biomicrofluidics 14 (2020) 41501.

[31] I. Raimondi, L. Izzo, M. Tunesi, M. Comar, D. Albani, C. Giordano, Organ-on-A-chip in vitro models of the brain and the blood-brain barrier and their value to study the microbiota-gut-brain Axis in neurodegeneration, Front. Bioeng. Biotechnol. 7 (2020) 435.

[32] H.E. Abaci, K. Gledhill, Z. Guo, A.M. Christiano, M.L. Shuler, Pumpless microfluidic platform for drug testing on human skin equivalents, Lab Chip 15 (2015) 882–888.

[33] I. Maschmeyer, A.K. Lorenz, K. Schimek, T. Hasenberg, A.P. Ramme, J. Hübner, M. Lindner, C. Drewell, S. Bauer, A. Thomas, N.S. Sambo, F. Sonntag, R. Lauster, U. Marx, A four-organ-chip for interconnected long-term co-culture of human intestine, liver, skin and kidney equivalents, Lab Chip 15 (2015) 2688–2699.

[34] I. Wagner, E.M. Materne, S. Brincker, U. Süßbier, C. Frädrich, M. Busek, F. Sonntag, D.A. Sakharov, E.V. Trushkin, A.G. Tonevitsky, R. Lauster, U. Marx, A dynamic multi-organ-chip for long-term cultivation and substance testing proven by 3D human liver and skin tissue co-culture, Lab Chip 13 (2013) 3538–3547.

[35] B. Ataç, I. Wagner, R. Horland, R. Lauster, U. Marx, A.G. Tonevitsky, R.P. Azar, G. Lindner, Skin and hair on-a-chip: in vitro skin models versus ex vivo tissue maintenance with dynamic perfusion, Lab Chip 13 (2013) 3555–3561.

[36] Q. Ramadan, F.C.W. Ting, In vitro micro-physiological immune-competent model of the human skin, Lab Chip 16 (2016) 1899–1908.

[37] I. Maschmeyer, T. Hasenberg, A. Jaenicke, M. Lindner, A.K. Lorenz, J. Zech, L.-A. Garbe, F. Sonntag, P. Hayden, S. Ayehunie, R. Lauster, U. Marx, E.-M. Materne, Chip-based human liver–intestine and liver–skin co-cultures – a first step toward systemic repeated dose substance testing in vitro, Eur. J. Pharm. Biopharm. 95 (2015) 77–87.

[38] B.S. Kim, J.-S. Lee, G. Gao, D.-W. Cho, Direct 3D cell-printing of human skin with functional transwell system Biofabrication 9 (2017) 25034.

[39] H.E. Abaci, Z. Guo, Y. Doucet, J. Jacków, A. Christiano, Next generation human skin constructs as advanced tools for drug development, Exp. Biol. Med. 242 (2017) 1657–1668.

[40] X. Ma, J. Liu, W. Zhu, M. Tang, N. Lawrence, C. Yu, M. Gou, S. Chen, 3D bioprinting of functional tissue models for personalized drug screening and in vitro disease modeling, Adv. Drug Deliv. Rev. 132 (2018) 235–251.

[41] G. Sriram, M. Alberti, Y. Dancik, B. Wu, R. Wu, Z. Feng, S. Ramasamy, P. L. Bigliardi, M. Bigliardi-Qi, Z. Wang, Full-thickness human skin-on-chip with enhanced epidermal morphogenesis and barrier function, Mater. Today 21 (2018) 326–340.

[42] I. Lorthois, M. Simard, S. Morin, R. Pouliot, Infiltration of T cells into a three-dimensional psoriatic skin model mimics pathological key features, Int. J. Mol. Sci. 20 (2019) 1670.

[43] J. Zhu, H.E. Abaci, Human skin-on-a-chip for mpox pathogenesis studies and preclinical drug evaluation, Trends in Pharmacological, Sciences 44 (2023) 865–868.

[44] S. Jeong, J. Kim, H.M. Jeon, K. Kim, G.Y. Sung, Development of an aged full-thickness skin model using flexible skin-on-a-chip subjected to mechanical stimulus reflecting the circadian rhythm, Int. J. Mol. Sci. 22 (2021) 12788.

[45] M. Ejiugwo, Y. Rochev, G. Gethin, G. O'Connor, Toward developing immunocompetent diabetic foot ulcer-on-a-chip models for drug testing Tissue Engineering Part C 27 (2021) 77–88.

[46] A.R. Vaughn, A. Branum, R.K. Sivamani, Effects of turmeric (Curcuma longa) on skin health: a systematic review of the clinical evidence, Phytother Res. 30 (2016) 1243–1264.

[47] K. Kim, J. Kim, H. Kim, G.Y. Sung, Effect of α-lipoic acid on the development of human skin equivalents using a pumpless skin-on-a-chip model, Int. J. Mol. Sci. 22 (2021) 2160.

[48] M.J. Garland, K. Migalska, T.-M. Tuan-Mahmood, T. Raghu Raj Singh, R. Majithija, E. Caffarel-Salvador, C.M. McCrudden, H.O. McCarthy, A. David Woolfson, R. F. Donnelly, Influence of skin model on in vitro performance of drug-loaded soluble microneedle arrays, Int. J. Pharm. 434 (2012) 80–89.

[49] N.R. Barros, H.J. Kim, M.J. Gouidie, K. Lee, P. Bandaru, E.A. Banton, E. Sarikhani, W. Sun, S. Zhang, H.J. Cho, M.C. Hartel, S. Ostrovidov, S. Ahadian, S.M. Hussain, N. Ashammakhi, M.R. Dokmeci, R.D. Herculano, J. Lee, A. Khademhosseini, Biofabrication of endothelial cell, dermal fibroblast, and multilayered keratinocyte layers for skin tissue engineering, Biofabrication 13 (2020) 035030.

[50] R.R. Wickett, M.O. Visscher, Structure and function of the epidermal barrier, Am. J. Infect. Control 34 (2006) S98–S110.

[51] P. Dardano, M. Battisti, I. Rea, L. Serpico, M. Terracciano, A. Cammarano, L. Nicolais, L. De Stefano, Polymeric microneedle arrays: versatile tools for an innovative approach to drug administration adv, Ther 2 (1900036) (2019).

[52] A. Singh, S. Yadav, Microneedling: advances and widening horizons Indian, Dermatol. Online J. 7 (2016) 244–254.

[53] H. Yousef, M. Alhajj, A.O. Fakoya, S. Sharma. Anatomy, Skin (Integument), EpidermisStatPearls, StatPearls Publishing, June 2024.

[54] Y. Guo, et al., Keratin 14-dependent disulfides regulate epidermal homeostasis and barrier function via 14-3-3σ and YAP1, Elife 9 (2020) e53165.

[55] M.A. McAleer, A.D. Irvine, The multifunctional role of filaggrin in allergic skin disease, J. Allergy Clin. Immunol. 131 (2013) 280–291.

[56] J.Y. Hong, T.-R. Kwon, J.H. Kim, B.C. Lee, B.J. Kim, Prospective, preclinical comparison of the performance between radiofrequency microneedling and microneedling alone in reversing photoaged skin, J. Cosmet. Dermatol. 19 (2019) 1105–1109.

[57] C.J. Dalton, C.A. Lemmon, Fibronectin: molecular structure, fibrillar structure and mechanochemical signaling Cells 10 (2021) 2443.

[58] S. Spada, et al., Fibronectin as a multiregulatory molecule crucial in tumor matrisome: from structural and functional features to clinical practice in oncology J, Exp. Clin. Cancer Res. 40 (2021) 102.

[59] V. Ivanova, Fibronectins: structural-functional relationships, J. Evol. Biochem. Physiol. 53 (2017) 450–464.

[60] R.B. Diller, A.J. Tabor, The role of the extracellular matrix (ECM) in wound healing: a review Biomimetics 7 (2022) 87.

[61] D. Singh, V. Rai, D.K. Agrawal, Regulation of collagen I and collagen III in tissue injury and regeneration Cardiol, Cardiovasc. Med. 7 (5) (2023).

[62] P.O. Staff, Correction: full-length fibronectin drives fibroblast accumulation at the surface of collagen microtissues during cell-induced tissue morphogenesis PLoS, Onearth 11 (2016) e0165354.

[63] Y. Poumay, F. Dupont, S. Marcoux, M. Leclercq-Smekens, M. Hérin, A. Coquette, A simple reconstructed human epidermis: preparation of the culture model and utilization in in vitro studies, Arch. Dermatol. Res. 296 (2004) 203–211.

[64] J. Scheurer, B. Sauer, J. Focken, M. Giampetraglia, A. Jäger, C.M. Schürch, B. Weigelin, B. Schittek, Histological and functional characterization of 3D human skin models mimicking the inflammatory skin diseases psoriasis and atopic dermatitis Disease Models & Mechanisms 17 (2024).

[65] C.C. Liao, C.Y. Wu, M.H. Lin, F.K. Hsieh, L.T. Hsu, S.Y. Chang, K.J. Chen, H. T. Huang, H.C. Hsu, C.H. Lin, P.J. Lin, Validation study of a new reconstructed human epidermis model EPiTRI for in vitro skin irritation test according to OECD guidelines, Toxicol. Vitro 75 (2021) 105197.

[66] F. Boraldi, F.D. Lofaro, S. Bonacorsi, A. Mazzilli, M. Garcia-Fernandez, D. Quaglino, The Role of Fibroblasts in Skin Homeostasis and Repair Biomedicines 12 (2024) 1586.

[67] P.C. Smith, C. Martínez, J. Martínez, C.A. McCulloch, Role of fibroblast populations in periodontal wound healing and tissue remodeling, Front. Physiol. 10 (2019) 270.

[68] J.M. Sorrell, A.I. Caplan, Fibroblast heterogeneity: more than skin deep, J. Cell Sci. 117 (2004) 667–675.

[69] J. Lee, A.A. Abdeen, K.L. Wycislo, T.M. Fan, K.A. Kilian, Interfacial geometry dictates cancer cell tumorigenicity, Nat. Mater. 15 (2016) 856.

[70] Z. Luo, W. Sun, J. Fang, K. Lee, S. Li, Z. Gu, M.R. Dokmeci, A. Khademhosseini, Biodegradable gelatin methacryloyl microneedles for transdermal, Drug Delivery Adv. Healthc. Mater. 8 (2019) 1801054.

[71] A.N. Linders, I.B. Dias, T. López Fernández, C.G. Tocchetti, N. Bomer, P. Van der Meer, A review of the pathophysiological mechanisms of doxorubicin-induced cardiotoxicity and aging, Aging 10 (9) (2024).

[72] A.K. Jain, C.H. Lee, H.S. Gill, 5-Aminolevulinic acid coated microneedles for photodynamic therapy of skin tumors, J. Contr. Release 239 (2016) 72–81.

[73] Y. Hao, Y. Chen, M. Lei, T. Zhang, Y. Cao, J. Peng, L. Chen, Z. Qian, Near-infrared responsive PEGylated gold nanorod and doxorubicin loaded dissolvable hyaluronic

acid microneedles for human epidermoid cancer therapy, Adv. Ther. 1 (2018) 1800008.
[74] R.F. Donnelly, M.R. Prausnitz, The promise of microneedle technologies for drug delivery Drug Deliv, Transl. Res. 14 (2023) 573–580.
[75] K. Ita, Transdermal delivery of drugs with microneedles-potential and challenges, Pharmaceutics 7 (2015) 90–105.